

Magnetohydrodynamic Simulation of the Interaction between Interplanetary Strong Shock and Magnetic Cloud and its Consequent Geoeffectiveness 2: Oblique Collision

Ming Xiong, Huinan Zheng, Yuming Wang, and Shui Wang

CAS Key Laboratory for Basic Plasma Physics, School of Earth and Space Sciences, University of Science and Technology of China, Hefei, Anhui 230026, China

arXiv:0904.0766v1 [astro-ph.SR] 5 Apr 2009

Ming Xiong, Huinan Zheng, Yuming Wang, and Shui Wang, CAS Key Laboratory for Basic Plasma Physics, School of Earth and Space Sciences, University of Science and Technology of China, Hefei, Anhui 230026, China (mxiong@mail.ustc.edu.cn; hue@ustc.edu.cn; ymwang@ustc.edu.cn; and swan@ustc.edu.cn)

Abstract. Numerical studies of the interplanetary “shock overtaking magnetic cloud (MC)” event are continued by a 2.5 dimensional magnetohydrodynamic (MHD) model in heliospheric meridional plane. Interplanetary direct collision (DC)/oblique collision (OC) between an MC and a shock results from their same/different initial propagation orientations. For radially erupted MC and shock in solar corona, the orientations are only determined respectively by their heliographic locations. OC is investigated in contrast with the results in DC [Xiong et al., 2006]. The shock front behaves as a smooth arc. The cannibalized part of MC is highly compressed by the shock front along its normal. As the shock propagates gradually into the preceding MC body, the most violent interaction is transferred sideways with an accompanying significant narrowing of the MC’s angular width. The opposite deflections of MC body and shock aphelion in OC occur simultaneously through the process of the shock penetrating the MC. After the shock’s passage, the MC is restored to its oblate morphology. With the decrease of MC-shock commencement interval, the shock front at 1 AU traverses MC body and is responsible for the same change trend of the latitude of the greatest geoeffectiveness of MC-shock compound. Regardless of shock orientation, shock penetration location regarding the maximum geoeffectiveness is right at MC core on the condition of very strong shock intensity. An appropriate angular difference between the initial eruption of an MC and an overtaking shock leads to the maximum deflection of the MC body. The larger the shock intensity is, the greater is the deflection angle. The interaction of MCs with other dis-

turbances could be a cause of deflected propagation of interplanetary coronal mass ejection (ICME).

1. Introduction

Interplanetary (IP) space is permeated by highly fluctuating solar wind with magnetic field frozen in its plasma [Parker, 1963]. The relatively quiet equilibrium of IP space is frequently interrupted by the solar disturbances, especially during solar maximum. Giant clouds of ionized gas with magnetic flux of 10^{23} maxwell and plasma mass of 10^{16} g, called coronal mass ejection (CME), are regularly emitted from the sun [Gosling, 1990; Webb et al., 1994]. IP CME (ICME) generally causes strong perturbation in the space environment as it passes by. Several models have already been applied in space weather forecasting, such as (1) HAF (Hakamada-Akasofu-Fry) [Fry et al., 2001, 2005]; (2) STOA (Shock Time of Arrival) [Smart and Shea, 1985]; (3) ISPM (Interplanetary Shock Propagation Model) [Smith and Dryer, 1990]; (4) an ensemble of HAF, STOA and ISPM models [Dryer et al., 2001, 2004]; (5) SWMF (Space Weather Modeling Framework) [Groth et al., 2000; Gombosi et al., 2001; Toth et al., 2005]; (6) HHMS (Hybrid Heliospheric Modeling System) [Detman et al., 2006] , and so on. Great challenges are still faced to improve the prediction performance of space weather to satisfy the ever-increasing demands from human civilization [Baker, 2002].

Magnetic clouds (MCs) are an important subset of ICMEs, whose fraction decreases from $\sim 100\%$ (though with low statistics) at solar minimum to $\sim 15\%$ at solar maximum [Richardson and Cane, 2004, 2005]. Identified by their characteristics including enhanced magnetic field, large and smooth rotation of magnetic field and low proton temperature [Burlaga et al., 1981], MCs have been the subject of increasingly intense study. The MCs with long interval of large southward magnetic field B_s are widely considered to

be the major IP origin of moderate to intense geomagnetic storms, especially during the solar maximum [Tsurutani, 1988; Gosling et al., 1991; Gonzalez et al., 1999] and, hence, play a crucial role in space weather prediction. An MC should probably be a curved loop-like structure with its feet connecting to the solar surface [Larson et al., 1997]. The force-free magnetic flux rope models have been proven to be very valuable to interpret in situ observations of MCs [Lundquist, 1950; Goldstein, 1983; Burlaga, 1988; Farrugia et al., 1993]. For the study of evolution of an individual MC during its anti-sunward propagation, many sophisticated models are developed based on these initial flux rope models: (1) Analytical models [Osherovich et al., 1993a, b, 1995; Hidalgo, 2003, 2005]; (2) Kinematic models [Riley and Crooker, 2004; Owens et al., 2006]; (3) Numerical models [Vandas et al., 1995, 1996, 1997, 2002; Groth et al., 2000; Odstrcil et al., 2002; Schmidt and Cargill, 2003; Manchester et al., 2004a, b]. Especially numerical simulations in (3) on a single MC have been exhaustive under the condition of various magnetic field strengths, axis orientations and speeds.

ICME is not an absolutely self-isolated entity during IP propagation. It may interact with other solar transients (e.g., shock, ejecta) and heterogenous medium (e.g., corotating interacting region). With less defined characteristics, some IP complex structures are reported recently, such as complex ejecta [Burlaga et al., 2002], multiple MCs [Wang et al., 2002a, 2003a], shock-penetrated MC [Wang et al., 2003b; Berdichevsky et al., 2005], non-pressure-balanced “MC boundary layer” associated with magnetic reconnection [Wei et al., 2003, 2006], ICME compressed by the following high-speed stream [Dal Lago et al., 2006], and so on. Dynamical response and ensuing geoeffectiveness of these structures are directly associated with the interaction during their formation and evolution. Numerical

simulations have been applied to study most of the complex structures: e.g., the interaction of a shock wave with an MC [Vandas et al., 1997; Odstrcil et al., 2003; Xiong et al., 2006], and the interaction of two MCs [Odstrcil et al., 2003; Gonzalez-Esparza et al., 2004; Lugaz et al., 2005; Wang et al., 2005].

The observed “shock overtaking MC” events substantiate the likelihood of strong shock propagation in low β medium of MC plasma and, therefore, present a very interesting topic in IP dynamics. The evolution stages of MC-shock interaction within 1 AU are determined by MC and shock commencement interval in solar corona. They can be assorted into two categories: (1) shock still in MC (e.g. October 3-6 2000 and November 5-7 2001 events [Wang et al., 2003b]); (2) shock ahead of MC after completely penetrating it (e.g. March 20-21 2003 event [Berdichevsky et al., 2005]). The idea that shock compression of the preexisting southward magnetic component can increase geoeffectiveness of the corresponding B_s event has been proved in data analyses [Wang et al., 2003d]. Particularly, MC-shock compounds in category (1) cause highly intense geomagnetic storms [Wang et al., 2003b, c; Xiong et al., 2006]. Furthermore the geoeffectiveness variance of MC-shock compound with respect to the increasing depth of a shock entering a preceding MC was investigated in our previous study [Xiong et al., 2006, hereinafter referred to as paper 1]. Both MC core and shock nose are radially erupted along heliospheric current sheet (HCS) in paper 1; however, the above-mentioned specific MC-shock events [Wang et al., 2003b; Berdichevsky et al., 2005] were all identified such that the shock flank sweeps the preceding MC body. IP direct collision (DC)/oblique collision (OC) of an MC and a shock results from their same/different initial propagation orientation. For radially erupted MC and shock in solar corona, the orientations are only determined respectively by the heli-

ographic locations of MC core and shock nose. Because the probability of MC core and shock nose radially launching from the same heliographic location is very rare and shock front extends over a wide angular span in IP medium, it is meaningful to study the role of shock orientation relative to a preceding MC propagation. DC in paper 1 is here modified to be OC for MC-shock interaction. The shock in DC/OC is correspondingly named as “central”/“non-central” shock. Moreover DC/OC is likely to be the IP interaction of two radially propagating disturbances from the same/different solar activity regions.

Section 2 presents a brief description of numerical magnetohydrodynamic (MHD) model. Section 3 discusses the dynamical evolution of MC-shock OC. Section 4 analyzes the ensuing geoeffectiveness of MC-shock compound. Section 5 describes the dependence of shock-induced MC deflection on shock orientation and intensity. Section 6 summarizes the conclusions.

2. Numerical MHD Model

The detailed description of the numerical model, including numerical scheme, computational mesh layout, prescription of the ambient solar wind and preceding MC, is given in paper 1. Only the shock introduction among input parameters of numerical model is modified to simulate OC of MC-shock interaction in contrast with DC in paper 1.

An incidental fast shock, which is radially launched from the inner boundary, is prescribed by several parameters: its emergence time t_{s0} , the latitude of its nose θ_{sc} , the latitudinal width of its flank $\Delta\theta_s$, the maximum shock speed within its front v_s , the duration of growth, maintenance and recovery phases (t_{s1} , t_{s2} , t_{s3}). Some parameters are fixed in all simulation cases of paper 1 and here, i.e. $\Delta\theta_s = 6^\circ$, $t_{s1} = 0.3$ hour, $t_{s2} = 1$ hour, $t_{s3} = 0.3$ hour. The remaining parameters (t_{s0} , θ_{sc} , v_s) are independently chosen

to mimic different conditions of IP MC-shock interaction. t_{s0} is used to separate the MC and shock initialization in time for reproducing different evolutionary stages of MC-shock compound at 1 AU. θ_{sc} designates emergence orientation of shock nose relative to previous MC propagation. Since the preceding MC emerges from the heliospheric equator, $\theta_{sc} = 0^\circ$ and $\theta_{sc} \neq 0^\circ$, corresponding to the introduction of “central” and “non-central” shock, determine MC-shock DC and OC in IP space respectively. v_s describes the intensity of MC-shock interaction to some extent. All introduced shocks in our simulation are strong enough to be faster than the local magnetosonic speed at all time and, therefore, to prevent weak shock dissipation in MC medium.

3. Dynamics of MC-shock Interaction

All fifty simulation cases are assorted into five groups in Table 1. Groups of individual MC (IM), direct collision (DC), oblique collision (OC), shock orientation dependence (SOD), and shock intensity dependence (SID) are studied respectively, where Groups IM and DC have been addressed in detail in paper 1. Case P₁ is shared by Groups DC and SOD, and Case P₂ shared by Groups OC, SOD and SID. With the identical v_s of 1630 kms⁻¹ and variable t_{s0} from 3 hours to 41 hour, Groups DC and OC only differ in θ_{sc} for comparative study. By modifying θ_{sc} from 0° to 10°, “central” shock in DC is directed to be “non-central” one in OC. Further, the parametric studies of θ_{sc} from 0° to 45° in Group SOD and v_s from 947 kms⁻¹ to 3173 kms⁻¹ in Group SID are explored as a supplement to Groups DC and OC. Cases B₁ and B₂ with $t_{s0} = 41$ hours, and Cases C₁ and C₂ with $t_{s0} = 10$ hours are typical examples of MC-shock interaction in categories 1 and 2 referred in Section 1.

3.1. Case B₂

The process of MC-shock interaction of Case B₂ is visualized in Figure 1. Under each image are two corresponding radial profiles by cutting right through 0° (noted by Lat. = 0°) and southern 4.5° (white dashed lines in the images, noted by Lat. = 4.5°S) away from the equator. The magnitude of magnetic field in radial profile is given by subtracting its corresponding initial value of ambient equilibrium. The body of MC is identified to be enclosed by a white solid line in the images and between two dotted lines in attached profiles. Magnetic field configuration is superimposed upon the images. The incidental shock aphelion arrives at $90R_s$ (along Lat. = 4.5°S) in 50.4 hours meanwhile the MC core arrives at $160R_s$ (along Lat. = 0°), shown in Figure 1(a), (d) and (g). Impending collision can be pregnant from large radial speed difference between the preceding MC and the following shock, as indicated by radial bulk flow speed v_r of 830 km s^{-1} at shock front and 540 km s^{-1} at MC head from the profile of Lat. = 4.5°S (Figure 1(d)). Though the latitudinal span of its flank is 6° initially at inner boundary, the shock extends up to 40° quickly due to its very strong intensity, until it emerges into IP medium completely. The traverse of shock front across the equator leads to significant HCS warping seen clearly in Figure 1(b), which is consistent with previous results [Smith et al., 1998; Hu and Jia, 2001]. As shock emergence orientation is redirected, the morphology of IP shock changes from a concave (Figure 3(e) in paper 1) to a smooth arc (Figure 1(e) here). As a result, MC-shock interaction consequently changes from DC to OC. The shock just catches up with the inner boundary of MC at 66.9 hours (Figure 1(b), (e) and (h)). Due to strong magnetic field and low β plasma, the radial characteristic speed of fast mode wave c_f of the MC is abnormally high at 1 AU with 200 km s^{-1} in maximum at MC core and

100 kms^{-1} in minimum at MC boundary. The rare chance of shock survival in an MC medium explains why only a few “shock overtaking MC” events are observed in IP space. Across the tangent point between inner MC boundary and shock front exists a quite sharp slope of v_r , as clearly seen along $\text{Lat.} = 4.5^\circ\text{S}$. MC-shock interaction begins from this tangent point at 66.9 hours. Once a slow MC is within the very large latitudinal span of the overtaking shock front, it will be swept by the shock and, from then on, the evolution of MC and shock will be coupled with each other. The overwhelming shock significantly distorts MC morphology at 85.4 hours (Figure 1(c), (f) and (i)). Namely, the originally curved magnetic field lines become very flat. The collision is more violent along $\text{Lat.} = 4.5^\circ\text{S}$. A sharp discontinuity is conspicuously formed in the rear part of MC with $B - B|_{t=0} = 25 \text{ nT}$, $v_r = 620 \text{ kms}^{-1}$, and $c_f = 260 \text{ kms}^{-1}$ in maximum within highly compressed region.

3.2. Case C₂

In Case C₂, an earlier shock emergence ($t_{s0} = 10$ hours) allows the incidental shock to ultimately penetrate the MC body within the solar-terrestrial heliospheric range. Only the evolution of v_r is given in Figure 2 to show the concerned MC-shock complex structure. Though an MC generally behaves like a rigid body with a little elasticity, magnetic field lines of the simulated MC appear to be too vulnerable to be easily deformed in the face of an overwhelming shock. The shock is radially emitted with the strongest intensity at front nose. Hence shock front behaves as an oblique curve relative to heliospheric equator due to the propagation speed difference from shock nose to edge flank. The MC is highly compressed by the shock along its normal. The shock front looks like a smooth arc in MC medium. As it propagates gradually into the preceding MC body, the most violent

interaction is transferred sideways (heliolatitudinally in the present study). Due to net shock-input angular momentum during MC-shock OC, the MC core starts to deflect away from initial shock orientation when the shock enters MC core, as seen in the contrast of Figure 2(b) and (c). The overall MC body is also deflected to the north. The global MC body deflection is quantified by the deflection angle of its core. Once the shock completely penetrates the MC, the grip of shock force on the MC is substantially relaxed, and the MC is restored to the roughly ellipse morphology by its field line elasticity. Meanwhile, the MC loses its angular speed component by the relative difference between the radial ambient flow and the speed's value at the MC boundary and, then propagates radially along the deflected angle. The incidental shock is also simultaneously deviated with its aphelion in the opposite direction, until it finally merges with the MC-driven shock into a compound one. The bend of interplanetary magnetic field (IMF) lines is obvious near the south of MC boundary, seen from Figure 2(c).

Figure 3 shows the comparison among Cases A, C_1 , and C_2 about time-dependent parameters: (a) radial distance of MC core r_m , (b) MC radial span Sr , (c) MC angular span $S\theta$, (d) MC cross section area A , and (e) MC core deflection angle $D\theta_m$, where the solid, dashed and dashed-dotted curves denote Cases A, C_2 and C_1 respectively, and the three vertical delimiting lines (dotted, dashed and dotted) from left to right correspond to the occasion of shock encountering MC tail, core and head respectively. The MC in Case C_2 is largely compressed by the shock, beginning from 13 hours. The dependence of the compression of MC geometry on shock orientation is illustrated by the comparison in Figure 3(b)-(d). Sr is larger while $S\theta$ is smaller for Case C_2 in Group OC. Though $S\theta$ is little affected in Case C_1 when shock front is in MC body ($13 \text{ hrs} < t < 33 \text{ hrs}$),

it is significantly narrowed in Case C₂. And the MC cross section area A in Case C₂, which represents the overall influence of shock compression due to integration of factor Sr and $S\theta$, is a bit larger than that in Case C₁. Starting from being encountered by the following shock, MC core deflects up to -4.5° until shock front reaches MC head, as seen in Figure 3(e). Though total deflection angle of MC core (-4.5°) amounts to three computational grids of latitudinal spacing 1.5° , MC deflection, we think, is indeed physical solution. Due to rough subcell resolution in numerical computation, MC core deflection behaves as a false discrete quantum-like transition instead of a realistic smooth one. But it does not distort the fundamental physical characteristics in numerical simulation.

3.3. Multi-Cases Comparison

The propagation of MC-shock structure toward the earth can be detected by L1-orbiting spacecraft, which perform the sentinel duty in space weather alarm system. The montage of the evolution of MC-shock compound at L1 under three typical circumstances is visualized in Figure 4, where (a)-(c) correspond to Case R₁ from Group DC and Cases Q₂ and R₂ from Group OC. Though the farthest radial distances of shock front in the north and south of the equator are almost identical in Cases R₁ and Q₂, the shock intensity in the south in Case Q₂ is apparently stronger than its north counterpart. With a smaller emergence interval, the shock in Case R₂ merges completely with the MC-driven shock into a compound one and moves faster in the south by contrast of Figure 4(b) and (c). Moreover the asymmetry of compound shock front with respect to heliospheric equator occurs when the shock erupts sideways relative to the MC propagation. The final MC propagation is slightly deviated from heliospheric equator to northern 4.5° after being ultimately penetrated by the shock, as seen from Figure 4(b) and (c). The succedent

high speed flow right after the inner boundary of preceding MC in Group DC, mentioned in paper 1, does not exist in corresponding Group OC, which can be seen from contrast between Figure 4(a), (b), and (c). The shock front with $\theta_{sc} \neq 0^\circ$ has the oblique normal relative to the preceding MC propagation, so the disturbance of speed enhancement downstream of shock front in Group OC can completely bypass or penetrate the obstacle of MC body and merge with the MC-driven shock.

4. Geoeffectiveness Studies

The southward magnetic flux within the MC is located in its rear part. The geomagnetic effect of simulated B_s event is quantified by Dst index. The in-situ measurements by a hypothetical spacecraft at L1 are inputted to Burton formula [Burton et al., 1975] to calculate Dst , as applied by Wang et al. [2003c]; Xiong et al. [2006].

Near-HCS latitudinal dependence of Dst index in Cases A, B₂, and C₂ is plotted in Figure 5. The positive and negative latitudes are referred to southern and northern semi-heliosphere. With the MC core marked by Δ and MC boundary by \diamond , the solid, dashed, and dashed-dotted lines denote Cases A, B₂, and C₂ respectively. Geomagnetic storm has been obviously aggravated by shock overtaking MC. The minimum Dst are found to be -103 nT, -168 nT, and -140 nT in Cases A, B₂, and C₂, respectively. Cases B₂ and C₂ are discussed one by one against Case A. Firstly, geomagnetic storm in Case A is largely enhanced in Case B₂ within the latitudinal span influenced by the shock. The minimum Dst occurs at 3° rather than 0° (the latitude of MC core passage), because the former undergoes more violent compression. The geoeffectiveness remain unchanged within $\text{Lat.} < -5^\circ$. The asymmetry of shock propagation with respect to heliospheric equator leads to subsequent asymmetry of geoeffectiveness of the MC-shock compound.

Secondly, in Case C₂ the concave of the latitudinal distribution of Dst is shifted 4.5° to the north. The MC deflection is caused by “non-central” shock penetrating MC body, as interpreted in section 3.2. As a result, the southward passing magnetic flux decreases due to the northward deflection of MC, and the IMF bend south of the equator due to shock passage, seen from Figure 2(c), which are responsible for the increased and decreased Dst in $2.3^\circ < \text{Lat.} < 9.4^\circ$ and $9.4^\circ < \text{Lat.} < 15^\circ$ respectively, comparing with Case A. Therefore, as shock front propagates from the south (Case B₂) to the north (Case C₂) in MC medium, the latitude of minimum Dst consequently moves in the same direction.

All MC-shock interaction cases of Group OC are integrated to study further the dependence of Dst index on the penetration depth d_{Dst} of shock overtaking MC. d_{Dst} is defined as the radial distance between shock front and MC inner boundary along sun-MC core. Three in-situ observations in time sequence at L1 along heliospheric equator and $\pm 4.5^\circ$ aside are synthetically analyzed in Figure 6, where the three vertical delimiting lines (dotted, dashed and dotted) from left to right correspond to the cases of shock encountering the tail, the core and the front of MC at L1, respectively. From top to bottom are plotted (a) MC-shock emergence interval, noted by Dt , (b) the Dst index, (c) the minimum of dawn-dusk electric field VB_z , noted by $\text{Min.}(VB_z)$, (d) the interval between the commencement of $VB_z < -0.5$ mV/m and the corresponding Dst minimum, noted by Δt , (e) the minimum of southward magnetic component B_s , noted by $\text{Min.}(B_s)$, and (f) the maximum of magnetic field magnitude $\text{Max.}(B)$, respectively. The solid, dashed and dashed-dotted lines in Figure 6(b)-(f) correspond to the observations at $\text{Lat.}=0^\circ$, 4.5°S and 4.5°N , respectively. The separate MC and shock events are coupled together when $Dt < 50$ hours. The shock penetrates into the preceding MC more deeply with shorter

Dt . $\text{Min.}(B_s)$ and $\text{Min.}(VB_z)$ decline dramatically along $\text{Lat.} = 4.5^\circ\text{S}$ as d_{Dst} increases from 0 to $10R_s$, because the first tangent point between MC boundary and shock front is very near 4.5°S . Dst decreases monotonically within $0R_s < d_{Dst} < 23.5R_s$ until shock front reaches MC core. Once the shock front exceeds the MC core ($d_{Dst} > 23.5R_s$), the latter begins to deflect northward. Moreover when $d_{Dst} > 23.5R_s$, the greatest compression region by the shock front is within the MC anterior part or the MC-driven sheath, where magnetic field is northward and, hence, contributes little to geoeffectiveness. So the mitigated geoeffectiveness along 0° , 4.5°S and aggravated geoeffectiveness along 4.5°N coexist, as seen from $23.5R_s < d_{Dst} < 44.5R_s$ in Figure 6(b).

Based on the analyses of Figures 5 and 6, MC deflection by MC-shock OC plays a crucial role in geomagnetic storms. The minimum Dst and its corresponding latitude among Dst latitudinal distribution for every case of Group OC are assembled in Figure 7. With a given Dt , there exists a latitude where geoeffectiveness reaches its maximum (Figure 7 (a)). This specific Dst value is plotted as dashed line in Figure 7(b). The latitudinal distribution of individual MC event (Case A), serving as a background in contrast, is also plotted as solid line in Figure 7(b). The relative ratio of geoeffectiveness enhancement by the shock is presented in Figure 7(c) to quantify two curves difference in Figure 7(b). As Dt decreases from 48 hours to 3 hours, the latitude of maximum geoeffectiveness firstly remains constant with decreased Dst from -115 nT to -180 nT, enhanced ratio from 20% to 91%, then monotonically changes from 3° to -4.5° with gradually subdued geoeffectiveness, finally remains constant again with further increased Dst from -130 nT to -115 nT, decreased ratio from 50% to 30%. The minimum Dst (-185 nT) occurs at 2.3° when the shock front enters MC core right at 1 AU. In contrast with paper 1, the

maximum geoeffectiveness of MC-shock interaction in Group DC is the same as that in Group OC despite occurrence at different heliolatitudes.

5. MC and Shock Deflections

IP MC deflection mentioned in Section 3.2 is a key parameter for solar-terrestrial transportation process, because it concerns the preexisting condition of geomagnetic storms – whether an MC could encounter the earth. In order to explore reliance of MC core deflection angle on shock orientation and intensity, the results of Groups SOD and SID are illustrated in Figure 8. Because MC core continuously deflects on the condition of shock front being in MC medium, seen from Figure 3(e), all t_{s0} in Groups SOD and SID are chosen to be 10 hours to have MC completely penetrated for obtaining final invariant angular displacement of MC core $D\theta_m$. Dst in Figure 8 refers to the geoeffectiveness at certain latitude of passage of deflected MC core. Firstly for Group SOD with different θ_{sc} , two factors affect $D\theta_m$: (1) $\theta_{sc} \neq 0$ is a premise of MC core deflection; $D\theta_m = 0$ corresponds to $\theta_{sc} = 0$. (2) As θ_{sc} increases, shock flank section encountered by MC body is further away from shock nose and, hence weaker. The absolute value of deflection angle tends to be smaller due to the weakening of MC-shock collision. The maximum deflection of MC core ($D\theta_m = -4.5^\circ$) occurs at certain θ_{sc} ($10^\circ < \theta_{sc} < 15^\circ$). Meanwhile Dst increases monotonically as a function of θ_{sc} , up to the value of corresponding individual MC event. Secondly for Group SID with different v_s , both $D\theta_m$ and Dst decrease steadily as v_s increases. Moreover, the slopes of two curves in Figure 8(c) and (d) decrease steadily, very abrupt in $v_s = 1000$ km/s and become nearly horizontal when $v_s \geq 3000$ km/s. This saturation effect on $D\theta_m$ and Dst is caused by the concurring deflection of shock aphelion opposite to that of MC core mentioned in Section 3.2. So the divergent trend of deflection

angle between the MC body and the shock aphelion counteracts, more or less, the effect of increasing shock speed v_s on MC-shock collision.

The finding of MC deflection due to interaction with a shock is further discussed through comparison with other relevant models. (1) Vandas et al. [1996] proposed that an MC deflects during the propagation through IP medium with unipolar IMF. Magnetic reconnection between IMF and inherent MC field across one side of MC boundary causes the angular force unbalance and, hence, leads to angular deflection. The MC continuously deflects through IP space. The role of magnetic helicity is responsible for deflection mechanism [Vandas et al., 1996]. However, such deflection needs to be verified further, as the reconnection should not be so significant in the IP medium with low β ; (2) Wang et al. [2004] suggested that CMEs could be deflected as largely as several tens degrees in the propagation under the effects of background solar wind and spiral IMF. CME deflects from its onset until accelerated or decelerated to background solar wind, which is expected to be done within several tens solar radii [Wang et al., 2006b]. It can well interpret the observation fact of east-west asymmetry of solar source distribution of earth-encountered halo CMEs [Wang et al., 2002b] and why some eastern limb CMEs encountered the earth [Zhang et al., 2003] and some disk CMEs missed the earth [e.g., Schwenn et al., 2005; Wang et al., 2006a]; (3) Our model here gives that MC deflection only happens during the process of shock front penetrating MC body. The effect of shock pushing MC aside leads to the deviation of MC by several degrees at the most; (4) We conjecture that interaction between ICMEs may also be a cause of ICME deflection, and the deflection angle could be up to tens degrees, larger than that in (3). The propagation trajectory of CMEs mentioned above is deflected from an initial straight line in the IP medium. Both

deflections in (1) and (2) are caused by interaction between ambient solar wind and IP disturbance. In contrary, the deflection in (3) and (4) are ascribed to interaction between different IP disturbances, i.e. the collision between MC-shock or MC-MC. It may expect a significant effect on the possibility of CME hitting the earth in (1), (2), and (4), whereas the effect in (3) may be negligible because of the small deflection angle.

The deflection of shock aphelion in IP medium is a key factor in the near-earth prediction of shock arrival time. Hu [1998]; Hu and Jia [2001] stated that the deflection of shock aphelion results from joint effects of spiral IMF and heterogenous medium consisting of fast and slow solar wind. The deflection is also found here in OC of MC-shock. Starting from shock passage through MC medium, shock aphelion deflects toward the contrary trend of MC deflection until the shock totally merges with the MC-driven shock. The final shock aphelion as well as front morphology are distinct from those of isolated shock event. Both MC and shock undergo significant modification during the process of their collision.

6. Concluding Remarks and Discussions

For further understanding of the IP “shock overtaking MC” events [Wang et al., 2003b; Berdichevsky et al., 2005], the investigation of MC-shock interaction and consequent geo-effectiveness in paper 1 is continued by a 2.5-dimensional ideal MHD numerical model. The simulations find that shock eruption orientation relative to preceding MC propagation plays a crucial role in MC-shock interaction.

Firstly, MC-shock dynamical interaction is modeled. In order to reveal the effect of the shock orientation relative to preceding MC propagation, DC in paper 1 is here modified to be OC for MC-shock interaction under the condition of the same shock speed. The results

show that the shock front in MC-shock OC behaves as a smooth arc in MC medium. The cannibalized part of MC is highly compressed by the shock along its normal. As the shock propagates gradually into the preceding MC body, the most violent interaction is transferred sideways (in terms of heliolatitude) with an accompanying significant narrowing of the MC's angular width. The opposite deflections of MC body and incidental shock aphelion concur during the process of shock penetrating MC. MC deflection ends when the shock approaches MC head; Shock deflection stops when the shock completely merges with MC-driven shock. After shock passage the MC is restored to oblate morphology. The high speed flow right after MC inner boundary mentioned in paper 1 does not exist here on the condition of non-uniform orientation of initial MC and shock eruption.

Secondly, the geoeffectiveness of MC-shock OC is studied. Geoeffectiveness of an individual MC is largely enhanced by an incidental “non-central” shock. With the decrease of MC-shock commencement interval, shock front at 1 AU traverses MC body and is responsible for the same change trend of the latitude of the greatest geoeffectiveness of MC-shock compound. Among all cases with penetrating shock at various stages, the maximum geoeffectiveness occurs when the shock enters MC core right at 1 AU. Wang et al. [2003c] suggested that the maximum geomagnetic storm be caused by shock penetrating MC at a certain depth, and the stronger the incident shock is, the deeper is the position. Based on our numerical model, Wang's conclusion of shock penetration depth regarding the maximum geoeffectiveness [Wang et al., 2003c] may be supplemented that shock position is right at MC core on the condition of very strong shock.

Thirdly, the reliance of MC deflection on shock orientation and intensity is explored. The angular displacements of MC body and shock aphelion are ascribed to MC-shock OC.

An appropriate angular difference between the initial eruption of an MC and an overtaking shock leads to the maximum deflection of the MC body. The larger the shock intensity is, the greater is the deflection angle. The interaction of MCs with other disturbances could be a cause of ICME's deflected propagation.

Acknowledgments. This work was supported by the National Natural Science Foundation of China (40336052, 40404014, 40525014 and 40574063), and the Chinese Academy of Sciences (startup fund). M. Xiong was also supported by Innovative Fund of University of Science and Technology of China for Graduate Students (KD2005030).

References

- Baker, D.N. (2002), How to cope with space weather, *Science*, *297*, 1,486–1,487.
- Berdichevsky, D.B., I.G. Richardson, R.P. Lepping, and S.F. Martin (2005), On the origin and configuration of the 20 March 2003 interplanetary shock and magnetic cloud at 1 AU, *J. Geophys. Res.*, *110*, doi:10.1029/2004JA010662.
- Burlaga, L.F. (1988), Magnetic clouds and force-free fields with constant alpha, *J. Geophys. Res.*, *93*, 7,217-7,224.
- Burlaga, L.F., E. Sittler, F. Mariani, and R. Schwenn (1981), Magnetic loop behind an interplanetary shock: Voyager, helios, and IMP 8 observations, *J. Geophys. Res.*, *86(A8)*, 6,673–6,684.
- Burlaga, L.F., S.P. Plunkett, and O.C.St. Cyr (2002), Successive CMEs and complex ejecta, *J. Geophys. Res.*, *107*, doi:10.1029/2001JA000255.
- Burton, R.K., R.L. McPherron, and C.T. Russell (1975), An empirical relationship between interplanetary conditions and Dst, *J. Geophys. Res.*, *80*, 4,204.

- Dal Lago, A., et al. (2006), The 17-22 October (1999) solar-interplanetary-geomagnetic event: Very intense geomagnetic storm associated with a pressure balance between interplanetary coronal mass ejection and a high-speed stream, *J. Geophys. Res.*, *111*, A07S14, doi:10.1029/2005JA011394.
- Detman, T., Z. Smith, M. Dryer, C. D. Fry, C. N. Arge, and V. Pizzo (2006), A hybrid heliospheric modeling system: Background solar wind, *J. Geophys. Res.*, *111*, A07102, doi:10.1029/2005JA011430.
- Dryer, M., C.D. Fry, W. Sun, C. Deehr, Z. Smith, S.-I. Akasofu and M.D. Andrews (2001), Prediction in real time of the 2000 July 14 heliospheric shock wave and its companions during the ‘Bastille’ epoch, *Sol. Phys.*, *204*, 267–286.
- Dryer, M., Z. Smith, C.D. Fry, W. Sun, C.S. Deehr, and S.-I. Akasofu (2004), Real time shock arrival predictions during the “Halloween 2003 epoch”, *Space Weather*, *2*, S09001, doi:10.1029/2004SW000087.
- Farrugia, C.J., L.F. Burlaga, V.A. Osherovich, I.G. Richardson, M.P. Freeman, R.P. Lepping, and A.J. Lazarus (1993), A study of an expanding interplanetary magnetic cloud and its interaction with the earth’s magnetosphere - the interplanetary aspect, *J. Geophys. Res.*, *98(A5)*, 7,621-7,632.
- Fry, C.D., W. Sun, C.S. Deehr, M. Dryer, Z. Smith, S.-I. Akasofu, M. Tokumaru, and M. Kojima (2001), Improvements to the HAF solar wind model for space weather predictions, *J. Geophys. Res.*, *106(A10)*, 20,985–21,001.
- Fry, C.D., M. Dryer, W. Sun, C.S. Deehr, Z. Smith, T.R. Detman, A. Aran, D. Lario, B. Sanahuja, and S.-I. Akasofu (2005), Key links in space weather: forecasting solar-generated shocks and proton acceleration, *AIAA. J.*, *43(5)*, 987–993.

- Goldstein, H. (1983), On the field configuration in magnetic clouds, in *JPL Solar Wind Five*, edited by M. Neugebauer, pp. 731-733, NASA Conf. Publ. 2280, Washington D.C..
- Gombosi, T.I., D.L. DeZeeuw, C.P.T. Groth, K.G. Powell, C.R. Clauer, and P. Song (2001), From Sun to Earth: multiscale MHD simulations of space weather, in *Space weather, Geophys. Monogr. Ser.*, Vol. 125, edited by P. Song, H. J. Singer, and G. L. Siscoe, p. 169–176, AGU, Washington, D. C., 2001.
- Gonzalez, W.D., B.T. Tsurutani, and A.L.C. Gonzalez (1999), Interplanetary origin of geomagnetic storms, *Space Sci. Rev.*, 88, 529.
- Gonzalez-Esparza, A., A. Santillan, and J. Ferrer (2004), A numerical study of the interaction between two ejecta in the interplanetary medium: one- and two-dimensional hydrodynamic simulations, *Ann. Geophys.*, 22, 3,741–3,749.
- Gosling, J.T. (1990), Coronal mass ejections and magnetic flux ropes in interplanetary space, in *Physics of magnetic flux ropes*, edited by C.T. Russell, E.R. Priest, and L.C. Lee, *Geophys. Monogr. Ser.*, 58, P. 343, AGU.
- Gosling, J.T., D.J. McComas, J.L. Phillips, and S.J. Bame (1991), Geomagnetic activity associated with earth passage of interplanetary shock disturbances and coronal mass ejections, *J. Geophys. Res.*, 96, 731.
- Groth, C.P.T., D.L. De Zeeuw, T.I. Gombosi, and K.G. Powell (2000), Global three-dimensional MHD simulation of a space weather event: CME formation, interplanetary propagation, and interaction with the magnetosphere, *J. Geophys. Res.*, 105(A11), 25,053–25,078.
- Hidalgo, M.A. (2003), A study of the expansion and distortion of the cross section of magnetic clouds in the interplanetary medium, *J. Geophys. Res.*, 108(A8), 1320,

doi:10.1029/2002JA009818.

- Hidalgo, M.A. (2005), Correction to “A study of the expansion and distortion of the cross section of magnetic clouds in the interplanetary medium”, *J. Geophys. Res.*, *110*, A03207, doi:10.1029/2004JA010752.
- Hu, Y.Q. (1998), Asymmetric propagation of flare-generated shocks in the heliospheric equatorial plane, *J. Geophys. Res.*, *103(A7)*, 14,631–14,641.
- Hu, Y.Q., and X.Z. Jia (2001), Interplanetary shock interaction with the heliospheric current sheet and its associated structures, *J. Geophys. Res.*, *106(A12)*, 29,299–29,304.
- Larson, D.E., et al. (1997), Tracing the topology of the October 18-20, 1995, magnetic cloud with $\sim 0.1 - 10^2$ keV electrons *Geophys. Res. Lett.*, *24*(15), 1,911–1,914.
- Lugaz, N., W.B. Manchester IV, and T.I. Gombosi (2005), Numerical simulation of the interaction of two coronal mass ejections from sun to earth, *Astrophys. J.*, *634*, 651–662.
- Lundquist, S. (1950), Magnetohydrostatic fields, *Ark. Fys.*, *2*, 361–365.
- Manchester, W.B., T.I. Gombosi, I. Roussev, D.L. De Zeeuw, I.V. Sokolov, K.G. Powell, G. Toth, and M. Opher (2004a), Three-dimensional MHD simulation of a flux rope driven CME, *J. Geophys. Res.*, *109*, A01102, doi:10.1029/2002JA009672.
- Manchester, W.B., T.I. Gombosi, I. Roussev, A. Ridley, D.L. De Zeeuw, I.V. Sokolov, K.G. Powell, and G. Toth (2004b), Modeling a space weather event from the Sun to the Earth: CME generation and interplanetary propagation, *J. Geophys. Res.*, *109*, A02107, doi:10.1029/2003JA010150.
- Odstroil, D., J.A. Linker, R. Lionello, Z. Mikic, P. Riley, V.J. Pizzo, and J.G. Luhmann (2002), Merging of coronal and heliospheric numerical two-dimensional MHD models, *J. Geophys. Res.*, *107(A12)*, SSH 14-1, doi:10.1029/2002JA009334.

- Odstrcil, D., M. Vandas, V.J. Pizzo, P. MacNeice (2003), Numerical Simulation of Interacting Magnetic Flux Ropes, in *AIP Conf. Proc. 679, Solar Wind 10*, edited by M. Velli, R. Bruno, and F. Malara, p. 699-702.
- Osherovich, V.A., C.J. Farrugia, and L.F. Burlaga (1993a), Nonlinear evolution of magnetic flux ropes, 1. low-beta limit, *J. Geophys. Res.*, *98*, 13,225.
- Osherovich, V.A., C.J. Farrugia, and L.F. Burlaga (1993b), Dynamics of aging magnetic clouds, *Adv. Space Res.*, *13*, 57.
- Osherovich, V.A., C.J. Farrugia, and L.F. Burlaga (1995), Nonlinear evolution of magnetic flux ropes, 1. finite-beta plasma, *J. Geophys. Res.*, *100*, 12,307.
- Owens, M.J., V.J. Merkin, and P. Riley (2006), A kinematically distorted flux rope model for magnetic clouds, *J. Geophys. Res.*, *111*, A03104, doi:10.1029/2005JA011460.
- Parker, E.N (1963), *Interplanetary dynamical process*, Wiley-Interscience, New York.
- Richardson, I.G., and H.V. Cane (2004), The fraction of interplanetary coronal mass ejections that are magnetic clouds: Evidence for a solar cycle variation, *Geophys. Res. Lett.*, *31*, L18804, doi:10.1029/2004GL020958.
- Richardson, I.G., and H.V. Cane (2005), A survey of interplanetary coronal mass ejections in the near-Earth solar wind during 1996-2005, in *Solar Wind 11 / SOHO 16*, edited by B. Fleck, T.H. Zurbuchen, and H. Lacoste, p. 154.1.
- Riley, P., and N.U. Crooker (2004), Kinematic treatment of CME evolution in the solar wind, *Astrophys. J.*, *600*, 1,035–1,042.
- Schmidt, J.M., and P.J. Cargill (2003), Magnetic reconnection between a magnetic cloud and the solar wind magnetic field, *J. Geophys. Res.*, *108(A1)*, 1,023, doi:10.1029/2002JA009325.

- Schwenn, R., A. Dal Lago, E. Huttunen, and W.D. Gonzalez (2005), The association of coronal mass ejection with their effects near the earth, *Ann. Geophys.*, *23(3)*, 1,033–1,059.
- Smart, D.F., and M.A. Shea (1985), A simplified model for timing the arrival of solar flare-initiated shocks, *J. Geophys. Res.*, *90*, 183–190.
- Smith, Z., and M. Dryer (1990), MHD study of temporal and spatial evolution of simulated interplanetary shocks in the ecliptic plane within 1 AU, *Sol. Phys.*, *129*, 387–405.
- Smith, Z., D. Odstrcil, and M. Dryer (1998), A 2.5-dimensional MHD parametric study of interplanetary shock interactions with the heliospheric current sheet / heliospheric plasma sheet, *J. Geophys. Res.*, *103(A9)*, 20,581–20,589.
- Toth, G., et al. (2005), Space Weather Modeling Framework: A new tool for the space science community, *J. Geophys. Res.*, *110*, A12226, doi:10.1029/2005JA011126.
- Tsurutani, B.T., W.D. Gonzalez, F. Tang, S.I. Akasofu, and E.J. Smith (1988), Origin of interplanetary southward magnetic fields responsible for major magnetic storms near solar maximum (1978–1979), *J. Geophys. Res.*, *93*, 8,519.
- Vandas, M., S. Fischer, M. Dryer, Z. Smith, and T. Detman (1995), Simulation of magnetic cloud propagation in the inner heliosphere in two dimensions 1. A loop perpendicular to the ecliptic plane, *J. Geophys. Res.*, *100(A7)*, 12,285–12,292.
- Vandas, M., S. Fischer, M. Dryer, Z. Smith, and T. Detman (1996), Simulation of magnetic cloud propagation in the inner heliosphere in two dimensions 2. A loop parallel to the ecliptic plane and the role of helicity, *J. Geophys. Res.*, *101(A2)*, 2,505–2,510.
- Vandas, M., S. Fischer, M. Dryer, Z. Smith, T. Detman, and A. Geranios (1997), MHD simulation of an interaction of a shock wave with a magnetic cloud, *J. Geophys. Res.*,

102(A10), 22,295–22,300.

Vandas, M., D. Odstrcil, and S. Watari (2002), Three-dimensional MHD simulation of a loop-like magnetic cloud in the solar wind, *J. Geophys. Res.*, *107(A9)*, SSH 2-1, doi:10.1029/2001JA005068.

Wang, Y.M., S. Wang and P.Z. Ye (2002a), Multiple magnetic clouds in interplanetary space, *Sol. Phys.*, *211*, 333–344.

Wang, Y.M., P.Z. Ye, S. Wang, G.P. Zhou, and J.X. Wang (2002b), A statistical study on the geoeffectiveness of Earth-directed coronal mass ejections from March 1997 to December 2000, *J. Geophys. Res.*, *107(A11)*, 1340, doi:10.1029/2002JA009244.

Wang, Y.M., P.Z. Ye and S. Wang (2003a), Multiple magnetic clouds: Several examples during March - April, 2001, *J. Geophys. Res.*, *108(A10)*, 1370, doi:10.1029/2003JA009850.

Wang, Y.M., P.Z. Ye, S. Wang, and X.H. Xue (2003b), An interplanetary cause of large geomagnetic storms: Fast forward shock overtaking preceding magnetic cloud, *Geophys. Res. Lett.*, *30(13)*, 1,700, doi:10.1029/2002GL016861.

Wang, Y.M., P.Z. Ye, S. Wang, and M. Xiong (2003c), Theoretical analysis on the geoeffectiveness of a shock overtaking a preceding magnetic cloud, *Sol. phys.*, *216*, 295–310.

Wang, Y.M., C.L. Shen, S. Wang, and P.Z. Ye (2003d), An empirical formula relating the geomagnetic storm's intensity to the interplanetary parameters: $-V\bar{B}_z$ and Δt , *Geophys. Res. Lett.*, *30(20)*, 2,039, doi:10.1029/2003GL017901.

Wang, Y.M., C.L. Shen, S. Wang, and P.Z. Ye (2004), Deflection of coronal mass ejection in the interplanetary medium, *Sol. phys.*, *222*, 329–343.

- Wang, Y.M., H.N. Zheng, S. Wang, and P.Z. Ye (2005), MHD simulation on formation and propagation of multiple magnetic clouds in the heliosphere, *Astron. Astrophys.*, *434*, 309-316.
- Wang, Y.M., X.H. Xue, C.L. Shen, P.Z. Ye, S. Wang, and J. Zhang (2006a), Impact of major coronal mass ejections on geo-space during 2005 September 7-13, *Astrophys. J.*, *646*, 625.
- Wang, Y.M., M. Xiong, H.N. Zheng, C.L. Shen, X.H. Xue, P.Z. Ye, and S. Wang (2006b), Deflected propagation of CMEs in the interplanetary medium, *the 36th COSPAR, PSW1-0036-06*, Beijing, China.
- Webb, D.F., T.G. Forbes, H. Aurass, J. Chen, P. Martens, B. Rompolt, V. Rusin, S.F. Martin, and V. Gaizauskas (1994), Material ejection: Report of the flares 22 workshop held at Ottawa, Canada, May 1993, *Sol. Phys.*, *153*, 73.
- Wei, F., R. Liu, Q. Fan and X. Feng (2003), Identification of the magnetic cloud boundary layers, *J. Geophys. Res.*, *108*(A6), 1,263, doi:10.1029/2002JA009511.
- Wei, F., X. Feng, F. Yang and D. Zhong (2006), A new non-pressure-balanced structure in interplanetary space: Boundary layers of magnetic clouds, *J. Geophys. Res.*, *111*, A03102, doi:10.1029/2005JA011272.
- Xiong, M., H.N. Zheng, Y.M. Wang, and S. Wang (2006), Magnetohydrodynamic simulation of the interaction between interplanetary strong shock and magnetic cloud and its consequent geoeffectiveness, *J. Geophys. Res.*, (in press), doi:10.1029/2005JA011593.
- Zhang, J., K.P. Dere, R.A. Howard, and V. Bothmer (2003), Identification of solar sources of major geomagnetic storms between 1996 and 2000, *Astrophys. J.*, *582*, 520–533.

Figure Captions

Figure 1 The evolution of shock overtaking MC for Case B₂, with (a)-(c) magnetic field magnitude B , (d)-(f) radial flow speed v_r , and (g)-(i) radial characteristic speed of fast mode c_f . Below each image are two additional radial profiles along Lat.= 0° and 4.5°S. Note: radial profile of B is plotted by subtracting initial ambient value $B|_{t=0}$. The white solid line in each image denotes the MC boundary. Solid and dashed lines at each profile denote MC core and boundary.

Figure 2 The evolution of shock overtaking MC for Case C₂ with radial flow speed v_r . Only part of domain is adaptively plotted to highlight MC.

Figure 3 The time dependence of MC parameters: (a) radial distance of MC core r_m , (b) MC radial span Sr , (c) MC angular span $S\theta$, (d) MC cross section area A , and (e) MC core deflection angle $D\theta_m$. The solid, dashed and dashed-dotted curves denote individual MC event (Case A), MC-shock events (Case C₂, C₁). Three vertical delimiting lines (dotted, dashed and dotted) from left to right correspond to the occasion of shock encountering MC tail, core and head respectively.

Figure 4 The montage of radial flow speed v_r for the evolution of MC-shock compound at L1 under three conditions.

Figure 5 The comparison of latitudinal distribution of Dst index among individual MC event (Case A) and MC-shock events (Cases B₂ and C₂). The solid, dashed, and dashed-dotted lines denote Case A, B₂, C₂ respectively, with the mark Δ , \diamond for the passage of MC core and boundary. The positive and negative latitude are referred to southern and northern semi-heliosphere.

Figure 6 The parameter variances of MC-related geoeffectiveness as a function of d_{Dst} in Group OC. Here d_{Dst} refers to radial distance between shock front and MC inner boundary along sun-MC core. From left to right, three vertical lines (dotted, dashed, dotted) denote the occasions of shock just reaching MC tail, core, and front at L1 respectively. The mark \diamond and Δ denote corresponding results of Case B₂ and C₂. (a) Dt , MC-shock emergence interval, (b) Dst index, (c) $\text{Min.}(VB_z)$, the minimum of dawn-dusk electric field VB_z , (d) Δt , the interval between the commencement of $VB_z < -0.5$ mV/m and the corresponding Dst minimum, (e) $\text{Min.}(Bs)$, the minimum of southward magnetic component, and (f) $\text{Max.}(B)$, the maximum of magnetic magnitude. Solid, dashed and dashed-dotted lines in (b) to (f) correspond to observations along $\text{Lat.}=0^\circ$, 4.5°S and 4.5°N respectively.

Figure 7 The response of the latitude of maximum geoeffectiveness and accompanying Dst (dashed line in (b)) as the change of MC-shock interval Dt in Group OC. The latitudinal distribution of individual MC event (Case A) is denoted in solid line of (b) as background. The relative ratio of geoeffectiveness enhancement (c) by the shock is derived from two curves difference of (b).

Figure 8 The dependence of MC core deflection angle $D\theta_m$ and Dst at the specific latitude accompanying MC core passage, on shock eruption orientation θ_{sc} (Group SOD) and speed v_s (Group SID). The horizontal dashed lines in (b) and (d) denote corresponding Dst of individual MC event (Case A).

Table 1. Assortment of simulation cases of individual MC and MC-shock interaction

Group	Case	v_s (km/s)	θ_{sc} ($^\circ$)	t_{s0} (hour)	Comment
IM	A	-	-	-	Individual MC
DC	B ₁ , C ₁ , D ₁ , E ₁ , F ₁ , G ₁ , H ₁ , I ₁ , J ₁ , K ₁ , L ₁ , M ₁ , N ₁ , O ₁ , P ₁ , Q ₁ R ₁	1630	0	41, 10, 60, 50, 48, 46, 44, 38, 35, 32, 29, 26, 23, 20, 15, 6, 3	Direct Collision
OC	B ₂ , C ₂ , D ₂ , E ₂ , F ₂ , G ₂ , H ₂ , I ₂ , J ₂ , K ₂ , L ₂ , M ₂ , N ₂ , O ₂ , P ₂ , Q ₂ R ₂	1630	10	41, 10, 60, 50, 48, 46, 44, 38, 35, 32, 29, 26, 23, 20, 15, 6, 3	Oblique Collision
SOD	P ₁ , a, P ₂ , b, c, d, e, f, g	1630	0, 5, 10, 15, 20, 25, 30, 40 45	10	Shock Orientation Dependence
SID	h, i, P ₂ , j, k, l, m, n o	947, 1226, 1402, 1630, 1773, 1997, 2314, 2686, 3173	10	10	Shock Intensity Dependence

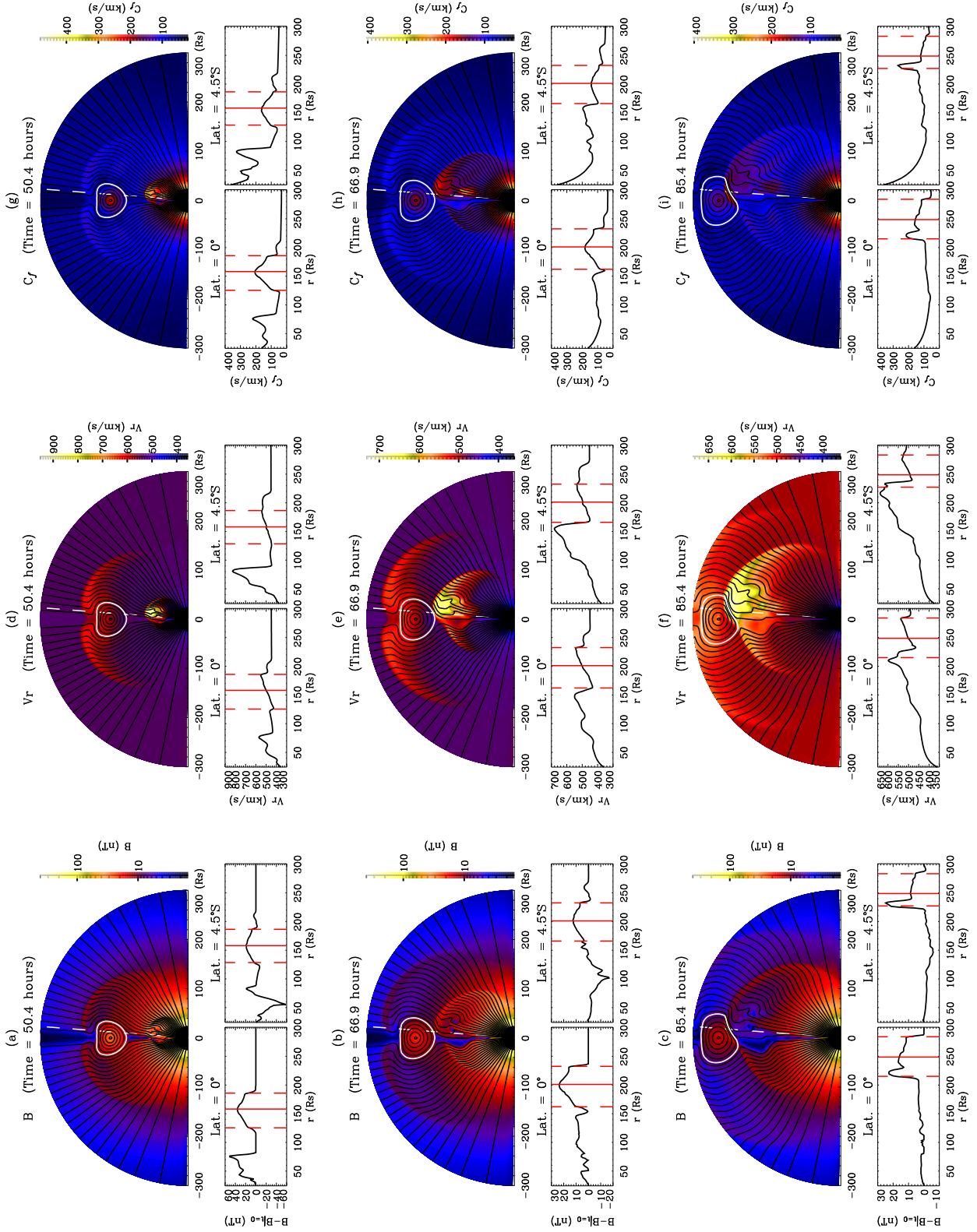


Figure 1.

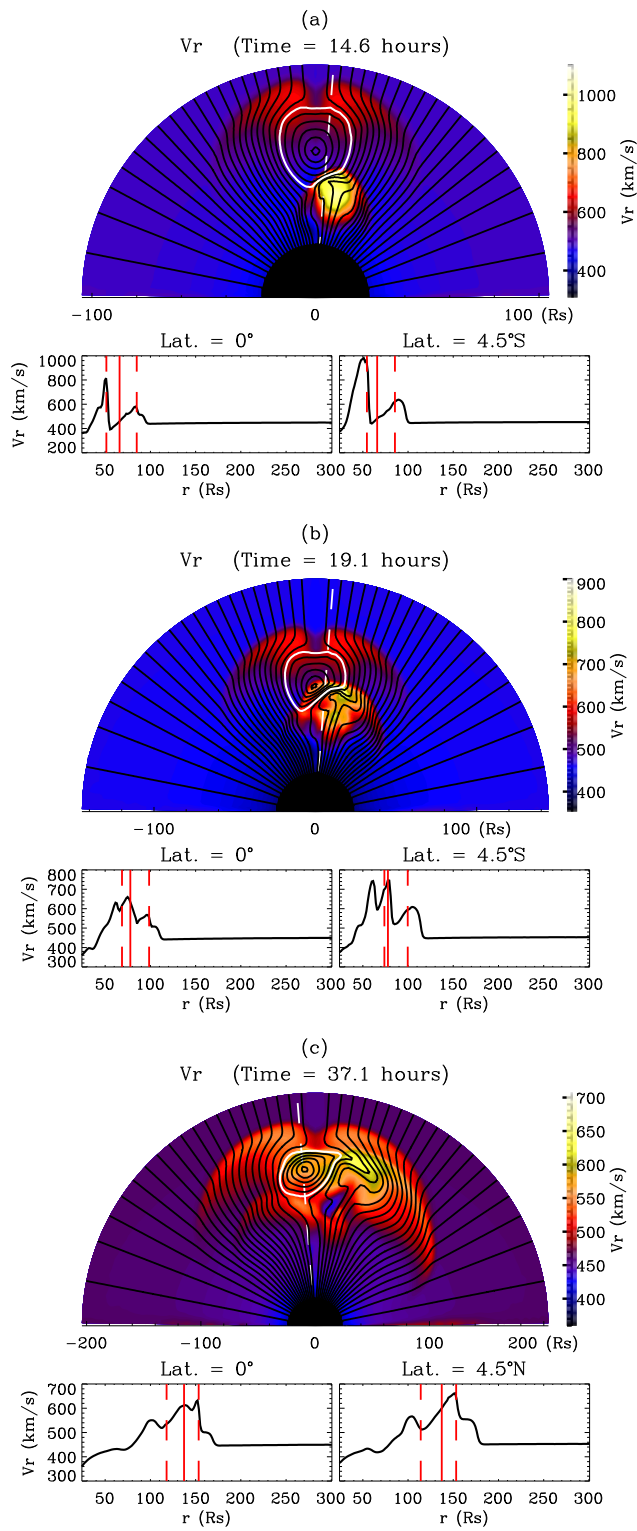


Figure 2.

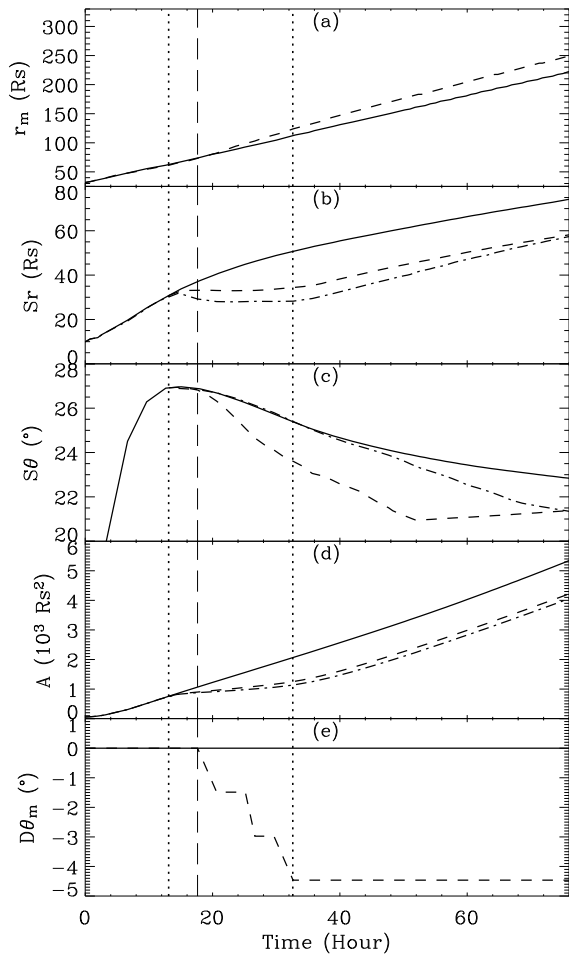


Figure 3.

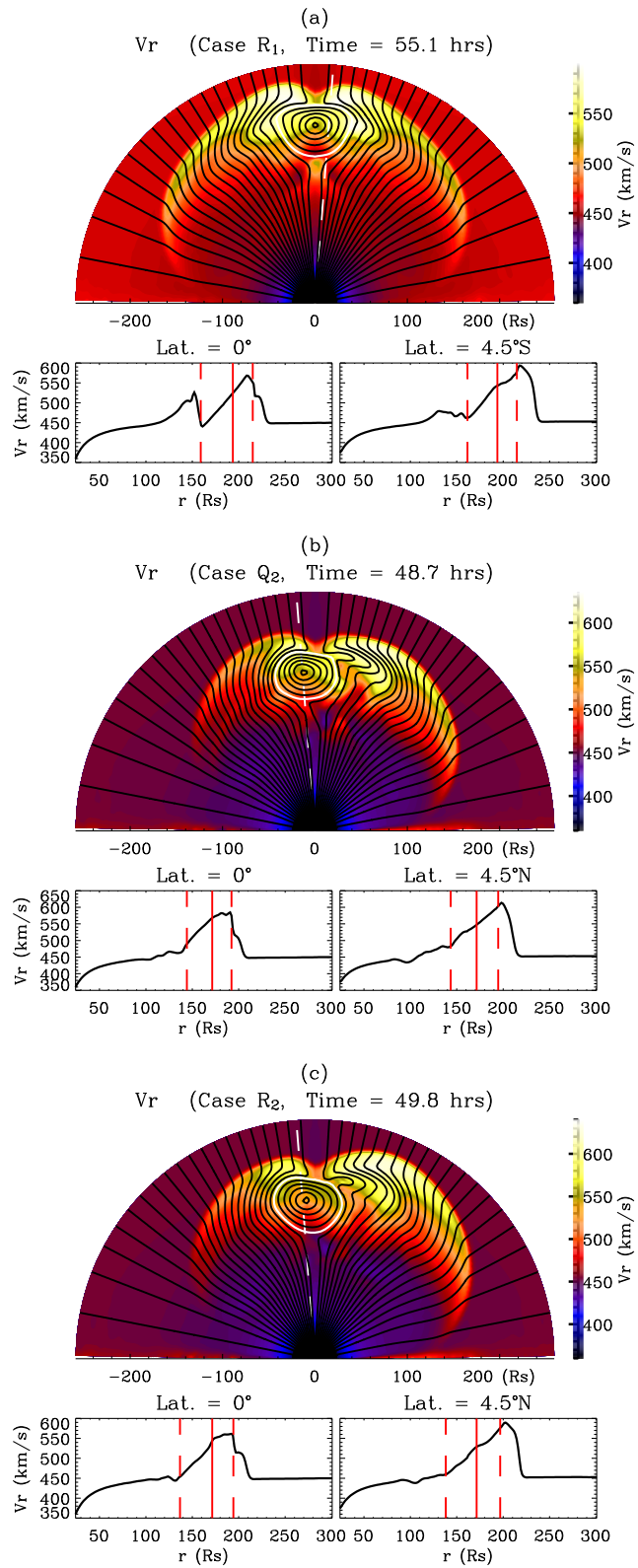


Figure 4.

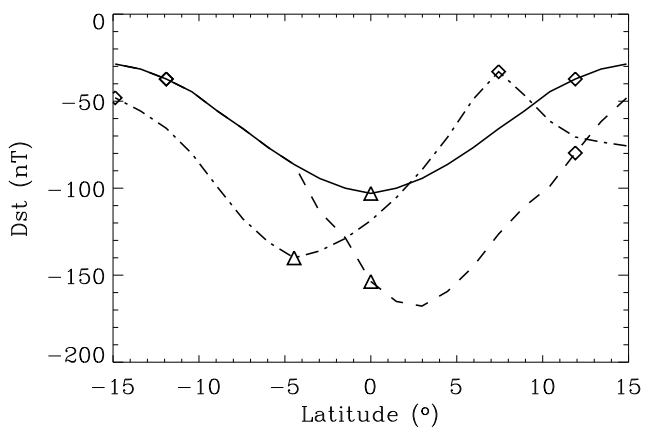


Figure 5.

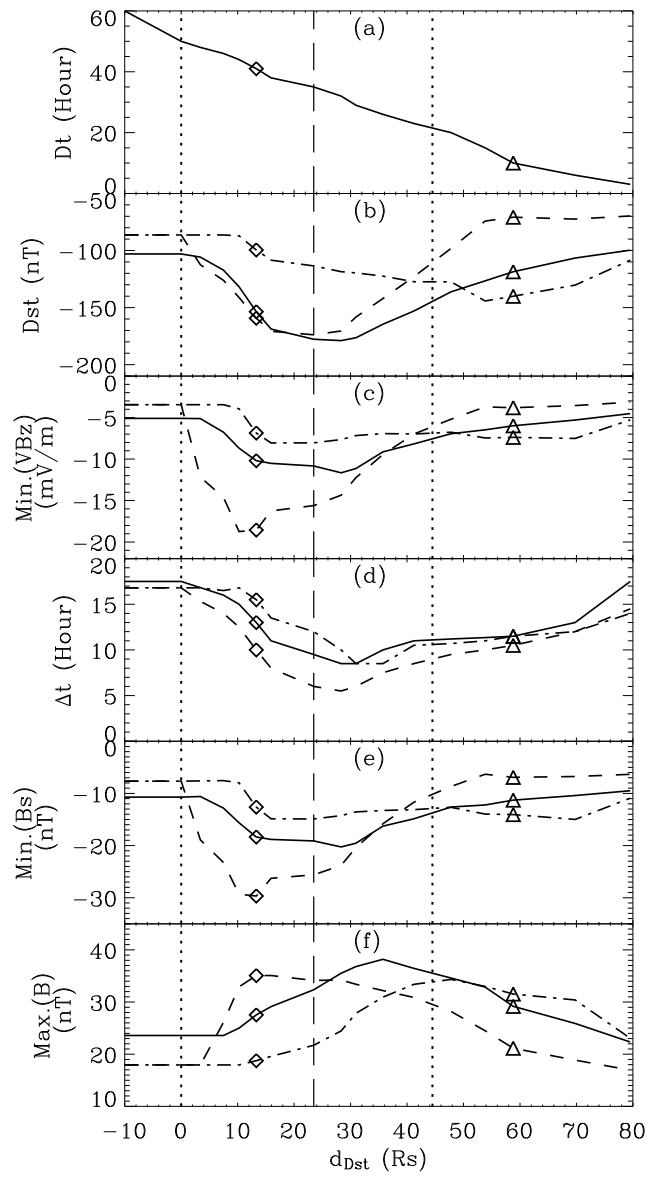


Figure 6.

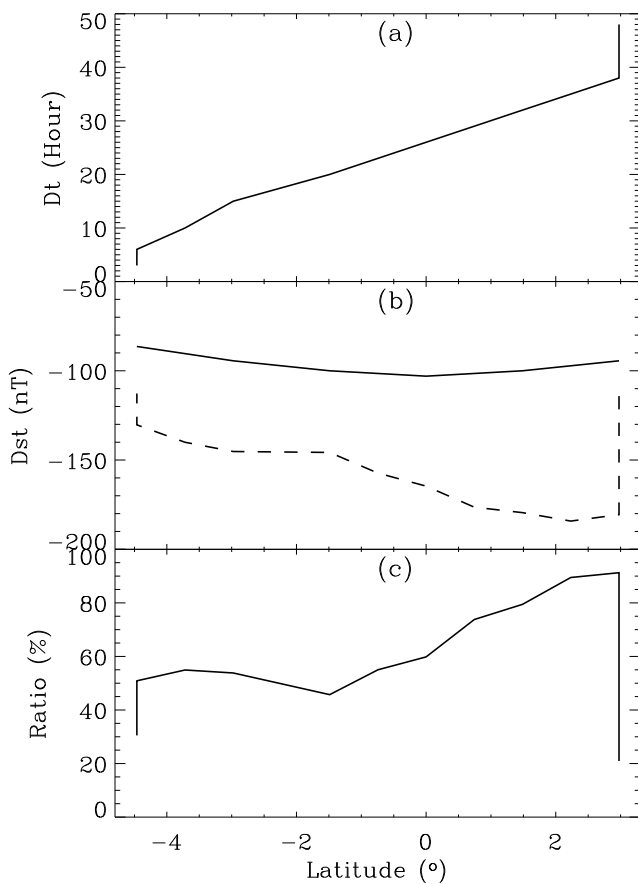


Figure 7.

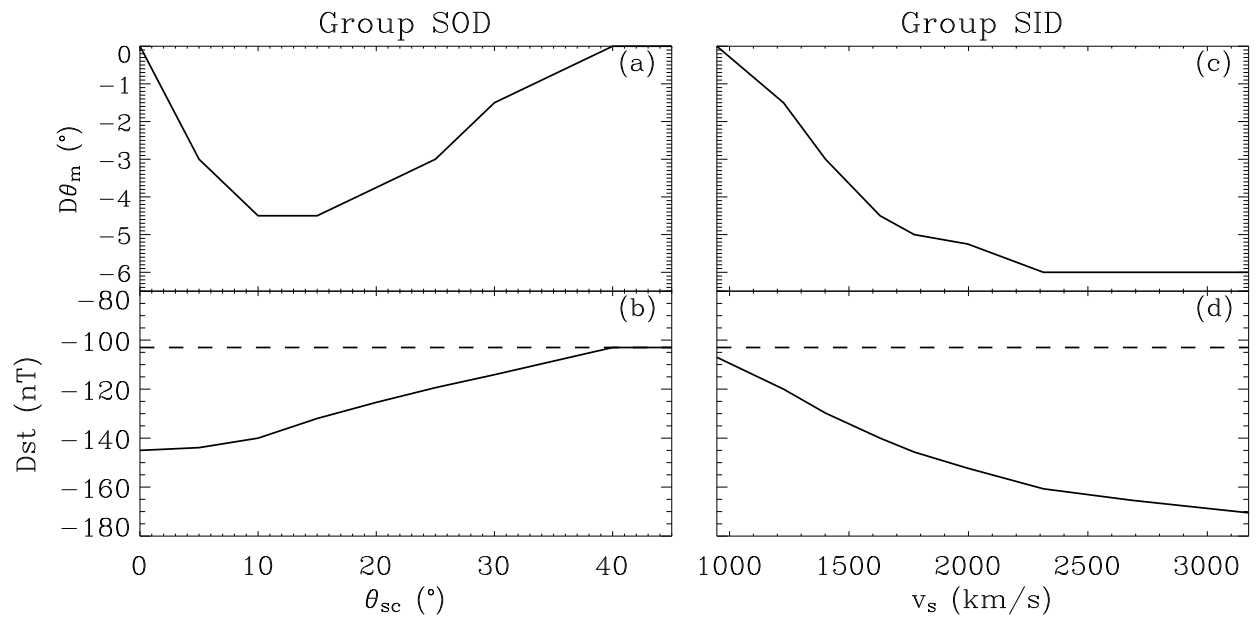


Figure 8.